The Astrophysical Journal, 719:728–736, 2010 August 10 doi:10.1088/0004-637X/719/1/728

ON THE ERUPTION OF CORONAL FLUX ROPES

Y. Fan
High Altitude Observatory, National Center for Atmospheric Research, 3080 Center Green Drive, Boulder, CO 80301, USA
Received 2010 June 1; accepted 2010 June 18; published 2010 July 22

ABSTRACT

We present three-dimensional MHD simulations of the evolution of the magnetic field in the corona where the emergence of a twisted magnetic flux tube is driven at the lower boundary into a pre-existing coronal potential arcade field. Through a sequence of simulations in which we vary the amount of twisted flux transported into the corona before the emergence is stopped, we investigate the conditions that lead to a dynamic eruption of the resulting coronal flux rope. It is found that the critical condition for the onset of eruption is for the center of the flux rope to reach a critical height at which the corresponding potential field declines with height at a sufficiently steep rate, consistent with the onset of the torus instability of the flux rope. In some cases, immediately after the emergence is stopped, the coronal flux rope first settles into a quasi-static rise with an underlying sigmoid-shaped current layer developing. Preferential heating of field lines going through this current layer may give rise to the observed quiescent X-ray sigmoid loops before eruption. Reconnections in the current layer during the initial quasi-static stage is found to add detached flux to the coronal flux rope, allowing it to rise quasi-statically to the critical height and dynamic eruption of the flux rope then ensues. By identifying field lines whose tops are in the most intense part of the current layer during the eruption, we deduce the evolution and morphology of the post-flare X-ray loops and the flare ribbons at their footpoints.

Key words: magnetic fields – magnetohydrodynamics (MHD) – methods: numerical – Sun: activity – Sun: corona – Sun: coronal mass ejections (CMEs)

Online-only material: animations

1. INTRODUCTION

It is now generally accepted that eruptive flares and coronal mass ejections (CMEs) correspond to a sudden, explosive release of the free magnetic energy stored in the previously quasi-equilibrium, twisted/sheared coronal magnetic field (see, e.g., review by Forbes et al. 2006). However, the detailed magnetic field structure for the eruption precursors and the physical causes for their sudden disruption remain fundamental unanswered questions under investigation. A wide range of CME models exists. Some models have considered sheared core fields for CME precursor structures (e.g., Mikić & Linker 1994; Antiochos et al. 1999), and others have considered twisted magnetic flux ropes containing helical field lines (e.g., Forbes & Priest 1995; Lin et al. 1998; Amari et al. 2000; Low 2001; Sturrock et al. 2001; Roussev et al. 2003; Török & Kliem 2005, 2007; Fan 2005; Fan & Gibson 2007; Isenberg & Forbes 2007). With regard to the causes for the onset of eruption, some models have considered ideal MHD instabilities and loss of equilibrium (e.g., Forbes & Priest 1995; Lin et al. 1998; Sturrock et al. 2001; Roussev et al. 2003; Török & Kliem 2005, 2007; Fan 2005; Kliem & Török 2006; Fan & Gibson 2007; Isenberg & Forbes 2007), and some of the others have considered a sudden enhancement of the rate of magnetic reconnection (e.g., Mikić & Linker 1994; Antiochos et al. 1999) as the trigger.

A coronal flux rope containing helical field lines twisting about each other by close to or more than one wind between the two ends anchored to the dense photosphere has been shown to be an appealing candidate for the basic underlying magnetic field structure for CME precursors (e.g., Titov & Demoulin 1999; Low 2001; Gibson & Fan 2006). Such coronal flux ropes can form as a result of active region flux emergence from the interior (e.g., Lites et al. 1995; Okamoto et al. 2008). MHD simulations in recent years suggest that a twisted subsurface flux tube does not rise bodily into the corona as a whole due to the heavy plasma that is trapped at the bottom concave portions of the helical field lines (e.g., Fan 2001; Archontis et al. 2004; Manchester et al. 2004; Fan 2009; Archontis & Hood 2010). Shear and rotational flows (corresponding to the observed sunspot rotations) on the photosphere driven by the Lorentz force of the twisted flux tube during flux emergence are the crucial means whereby twist is transported from the interior into the solar corona, leading to the formation and ascent of a coronal flux rope with a new axial field line, and containing sigmoid-shaped dipped field lines twisting about the axial field line (Manchester et al. 2004; Magara 2004, 2006; Archontis et al. 2009; Fan 2009; Archontis & Hood 2010). For quiescent filaments, it has been shown that coronal flux ropes can form as a result of photospheric supergranular diffusion in decaying active regions (e.g., van Ballegooijen et al. 1998, 2000; Mackay & van Ballegooijen 2001, 2005; Amari et al. 2003).

In this work, we focus on studying the conditions for the eruption of a three-dimensional (3D) line-tied corona flux rope. We carry out a sequence of simulations of the evolution of the magnetic field in the corona, where the emergence of a twisted flux tube is driven (kinematically) through the lower boundary into a pre-existing coronal arcade and where the emergence is stopped at variable times such that a different amount of twisted flux is driven into the corona. In these simulations, the imposed (kinematic) emergence of a twisted flux tube through the lower boundary may not reflect what realistically happens, but is a means to obtain a sequence of near-force-free coronal flux rope equilibria with an increasing amount of locally detached, twisted flux. In all of our simulated cases, a quasi-equilibrium of a line-tied coronal flux rope confined by the external arcade field is established immediately after the emergence is stopped and we follow the subsequent evolution. We find that in all cases, current layers of sigmoid morphology develop underlying the flux ropes during the quasi-static stage immediately after the

emergence is stopped. Magnetic reconnections in the current layer are found to continue to add detached, twisted flux to the flux rope during the initial quasi-static phase, even though the total magnetic energy decreases slowly due to the reconnections (and note that no more Poynting flux and helicity flux are being transported through the lower boundary since the flux emergence is stopped). This continued addition of the detached flux allows the flux rope to continue to rise quasi-statically. We find that a transition to dynamic eruption of the coronal flux rope takes place when it exceeds a critical height, where the corresponding potential field decreases with height at a sufficiently steep rate, consistent with the onset of the torus instability of the flux rope. This result indicates the fundamental role played by the torus instability in triggering an ejective eruption of a 3D line-tied coronal flux rope and suggests that the "tether-cutting" reconnections (Moore et al. 2001) in the pre-eruption sigmoid current layer during the initial quasi-static phase are means to bring the flux rope to the critical height. This is in agreement with the result of a previous, substantially different numerical model of a coronal flux rope driven by photospheric shear and flux cancellation by Aulanier et al. (2010), where they concluded that photospheric flux-cancellation and tether-cutting coronal reconnections do not trigger CMEs, but are key mechanisms for flux ropes to build up and to rise to the critical height where the torus instability causes the eruption.

2. MODEL DESCRIPTION

For the simulations carried out in this study, we solve the following isothermal MHD equations:

$$\frac{\partial \rho}{\partial t} + \nabla \cdot (\rho \mathbf{v}) = 0, \tag{1}$$

$$\rho \left(\frac{\partial \mathbf{v}}{dt} + (\mathbf{v} \cdot \nabla)\mathbf{v} \right) = -\nabla p - \rho \frac{GM_\odot}{r^2}\hat{\mathbf{r}} + \frac{1}{4\pi}(\nabla \times \mathbf{B}) \times \mathbf{B}, \tag{2}$$

$$\frac{\partial \mathbf{B}}{\partial t} = \nabla \times (\mathbf{v} \times \mathbf{B}), \tag{3}$$

$$\nabla \cdot \mathbf{B} = 0, \tag{4}$$

$$p = a_s^2 \rho, \tag{5}$$

in a spherical domain representing the solar corona, given by $r \in [R_\odot, 5.496\, R_\odot]$, $\theta \in [5\pi/12, 7\pi/12]$, $\phi \in [-\pi/9.6, \pi/9.6]$ (see the black box in Figure 1). In the above equations, $\mathbf{v}$, $\mathbf{B}$, ρ, p, a_s, G, $M_\odot$ denote, respectively, the velocity field, the magnetic field, the density, the pressure, the isothermal sound speed, the gravitational constant, and the mass of the Sun. The temperature of the isothermal corona is assumed to be $T_0 = 1$ MK, and thus the isothermal sound speed $a_s = 128$ km s^{-1}. The domain is resolved by a grid of $432 \times 192 \times 240$ which is uniform in θ and ϕ and non-uniform in r: in the range from $r = R_\odot$ to $r = 1.788\, R_\odot$, the grid size $dr = 0.0027271\, R_\odot = 1.898$ Mm, and dr increases gradually for $r > 1.788\, R_\odot$, reaching about $dr = 0.09316\, R_\odot$ at the outer boundary. The above isothermal MHD equations are discretized spatially in the spherical domain using a staggered finite-difference scheme (Stone & Norman 1992a) and advanced in time using an explicit, second-order accurate, two-step predictor-corrector time stepping. A modified, second-order accurate Lax-Friedrichs scheme as described in Rempel et al. (2009, see Equation (A3) in that paper) is used for evaluating the fluxes in the continuity equation for density. Compared to the standard second-order Lax-Friedrichs scheme, this scheme significantly reduces numerical diffusivity in regions of smooth variation, while retaining the same robustness in regions of discontinuities (such as shocks). The standard second-order Lax-Friedrichs scheme is used for evaluating the fluxes in the momentum equation. A method of characteristics that is upwind in the Alfvén waves (Stone & Norman 1992b) is used for evaluating the $\mathbf{v} \times \mathbf{B}$ term in the induction equation, and the constrained transport scheme is used to ensure $\nabla \cdot \mathbf{B} = 0$ to the machine precision.

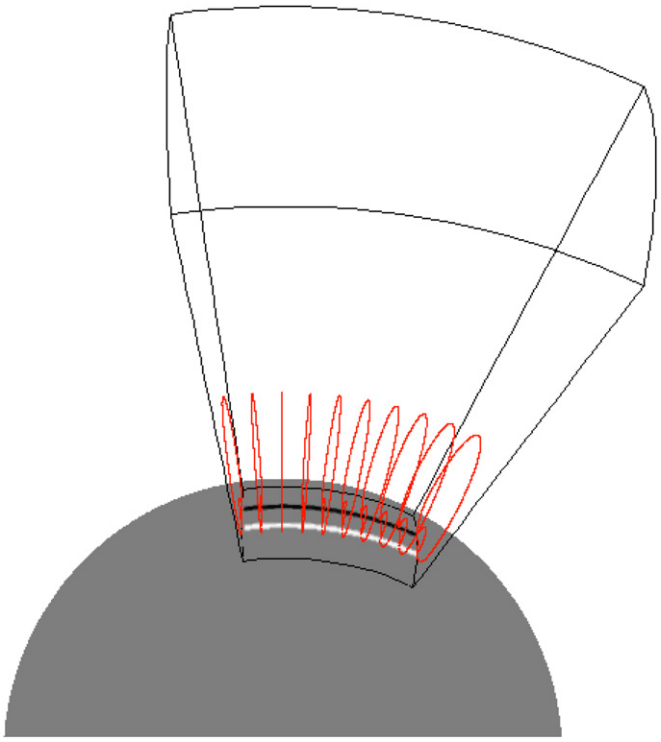

Figure 1. Initial configuration of the simulations (see the text for details).

Initially, the domain is assumed to be in the state of a hydrostatic isothermal atmosphere with the density and pressure given by

$$\rho = \rho_0 \exp\left(-\frac{R_\odot}{H_{p0}} \left(1 - \frac{R_\odot}{r} \right) \right) \tag{6}$$

$$p = \frac{RT_0 \rho}{\mu}. \tag{7}$$

The pressure scale height at the bottom of the domain, which corresponds to the base of the corona, is $H_{p0} = (RT_0/\mu)(GM_\odot/R_\odot^2)^{-1} = 60$ Mm. The density at the base is $\rho_0 = 8.365 \times 10^{-16}$ g cm^{-3}. The initial atmosphere contains a pre-existing potential arcade field (see the red field lines in Figure 1), whose normal field $B_r(0, \theta, \phi)$ at the lower boundary (see the gray-scale image on the sphere in Figure 1) is given by

$$B_r(0, \theta, \phi) = \frac{1}{R_\odot^2 \sin\theta} \frac{dA_s(\theta)}{d\theta}, \tag{8}$$

where

$$A_s(\theta)=\begin{cases}0, & \frac{5}{12}\pi<\theta<\frac{\pi}{2}-\theta_t-\theta_a,\\ -\frac{\theta_a}{\pi}\sin\theta_p B_0 R_\odot^2\left[1-\cos\left[\frac{\pi}{\theta_a}\left[\theta-\left(\frac{\pi}{2}-\theta_a-\theta_t\right)\right]\right]\right], & \frac{\pi}{2}-\theta_t-\theta_a<\theta<\frac{\pi}{2}-\theta_t,\\ -\frac{2\theta_a}{\pi}\sin\theta_p B_0 R_\odot^2, & \frac{\pi}{2}-\theta_t<\theta<\frac{\pi}{2}+\theta_t,\\ -\frac{\theta_a}{\pi}\sin\theta_p B_0 R_\odot^2\left[1+\cos\left[\frac{\pi}{\theta_a}\left[\theta-\left(\frac{\pi}{2}+\theta_t\right)\right]\right]\right], & \frac{\pi}{2}+\theta_t<\theta<\frac{\pi}{2}+\theta_t+\theta_a,\\ 0, & \frac{\pi}{2}+\theta_t+\theta_a<\theta<\frac{7}{12}\pi,\end{cases} \quad (9)$$

in which $\theta_a = 0.05$, $\theta_t = 0.0432$, $\theta_p = \pi/2 - \theta_t - \theta_a/2$, and $B_0 = 20$ G is the peak field strength in the arcade field. Thus, the peak Alfvén speed at the footpoint of the arcade field is $v_{A0} = B_0/\sqrt{4\pi\rho_0} = 1951$ km s^{-1} which is more than a factor of 10 greater than the isothermal sound speed a_s.

At the lower boundary of the domain at $r = R_\odot$, we impose (kinematically) the emergence of a twisted, arched flux tube $\mathbf{B}_{\rm tube}$ by specifying at the $r = R_\odot$ boundary a time-dependent transverse electric field $\mathbf{E}_\perp|_{r=R_\odot}$ that corresponds to the upward advection of the flux tube at a velocity $\mathbf{v}_0$:

$$\mathbf{E}_\perp|_{r=R_\odot} = \hat{\mathbf{r}}\times\left[\left(-\frac{1}{c}\mathbf{v}_0\times\mathbf{B}_{\rm tube}(R_\odot,\theta,\phi,t)\right)\times\hat{\mathbf{r}}\right]. \quad (10)$$

Here, the imposed velocity field on the lower boundary is a constant $\mathbf{v}_0$ in the area where the emerging tube intersects the lower boundary and zero in the rest of the area. The magnetic field $\mathbf{B}_{\rm tube}$ used for specifying $\mathbf{E}_\perp|_{r=R_\odot}$ is an axisymmetric torus defined in its own local spherical polar coordinate system (r', θ', ϕ') whose origin is located at $\mathbf{r} = \mathbf{r}_0 = (r_0, \theta_0, \phi_0)$ of the Sun's spherical coordinate system and whose polar axis is parallel to the polar axis of the Sun's spherical coordinate system:

$$\mathbf{B}_{\rm tube} = \nabla\times\left(\frac{A(r',\theta')}{r'\sin\theta'}\hat{\phi}'\right) + B_{\phi'}(r',\theta')\hat{\phi}', \quad (11)$$

where

$$A(r',\theta') = \frac{1}{2}qa^2B_t\exp\left(-\frac{\varpi^2(r',\theta')}{a^2}\right), \quad (12)$$

$$B_{\phi'}(r',\theta') = \frac{aB_t}{r'\sin\theta'}\exp\left(-\frac{\varpi^2(r',\theta')}{a^2}\right). \quad (13)$$

In the above equations, a is the minor radius of the torus, $\varpi = (r'^2 + R'^2 - 2r'R'\sin\theta')^{1/2}$ is the distance to the curved axis of the torus, where R' is the major radius of the torus, q denotes the angular amount (in rad) of field line rotation about the axis over a distance a along the axis, and $B_t a/R'$ gives the field strength at the curved axis of the torus. Here, we have $a = 0.04314\,R_\odot$, $R' = 0.25\,R_\odot$, $q/a = -0.0166$ rad Mm^{-1}, and $B_t a/R = 2.24B_0$. The magnetic field $\mathbf{B}_{\rm tube}$ is truncated to zero outside of the flux surface whose distance to the torus axis is $\varpi = a$. For specifying the flux emergence via $\mathbf{E}_\perp|_{r=R_\odot}$ given by Equation (10), it is assumed that the torus' center is initially located at $\mathbf{r}_0 = (r_0 = 0.707\,R_\odot,\ \theta_0 = \pi/2,\ \phi_0 = 0)$ (thus the torus is initially entirely below the surface) and it moves bodily toward the lower boundary at a constant velocity $\mathbf{v}_0 = v_0\hat{\mathbf{r}}_0$, with $v_0 = 0.001v_{A0}$, until a time $t_{\rm stp}$, when the emergence is stopped and $\mathbf{E}_\perp|_{r=R_\odot}$ is set to zero. Note that the coronal domain and the size of the driving emerging torus we use in this study are both about a factor of 2 smaller than those used in Fan & Gibson (2007), leading to flux ropes in the corona being more representative of the typical size of a coronal prominence/filament.

In this paper, we have performed a sequence of simulations where we vary the time $t_{\rm stp}$ when the emergence is stopped, so that a varying amount of the twisted flux of the torus is transported into the corona, to examine the critical condition for the onset of eruption of the coronal flux rope (see Table 1 for the parameters used for the different simulations). We assume that the density inside the torus entering the lower boundary is ρ_0 (same as the initial density at the bottom of the domain), and thus, during the imposed flux emergence, an inflow of mass flux $\rho_0 v_{0r}$ is also imposed at the lower boundary in the area where the emerging tube intersects the boundary (outside of this area on the lower boundary, the mass flux is zero). After the emergence is stopped, there is zero mass flux flowing through the lower boundary. Note that throughout the simulation, the density inside the domain is evolved naturally by solving the continuity equation, with an imposed lower boundary mass flux distribution, which is zero after the emergence is stopped. We assume perfectly conducting walls for the side boundaries of the simulation domain. For the outer boundary, we use a simple outward extrapolating boundary condition that allows plasma and magnetic field to flow through.

In the remainder of the paper, quantities are expressed in the following units unless otherwise specified: $R_\odot = 6.96\times10^{10}$ cm, $\rho_0 = 8.365\times10^{-16}$ g cm^{-3}, $B_0 = 20$ G, $v_{A0} = B_0/\sqrt{4\pi\rho_0} = 1.951\times10^8$ cm s^{-1}, and $\tau_{A0} = R_\odot/v_{A0} = 356.8$ s, as units for length, density, magnetic field, velocity, and time, respectively.

3. RESULTS

3.1. The Onset of Eruption

Figure 2 shows snapshots of the 3D coronal magnetic field evolution from two simulations, cases s1 and e1 in Table 1, for which the times $t_{\rm stp}$ at which the flux emergence is stopped only differ slightly ($t_{\rm stp} = 89.0$ for case s1 and $t_{\rm stp} = 89.125$ for case e1). The relative magnetic helicity (Berger & Field 1984) of the coronal magnetic field H_m reached at the time the emergence is stopped (given in the third column in Table 1) is thus also very close for the two cases (with the relative difference being only about 5×10^{-4}). Note that the relative magnetic helicity H_m is computed in the same way as described in Fan & Gibson (2007, see Equations (15), (A2), and (A3) in that paper). After the flux emergence is stopped at $t_{\rm stp}$, the coronal flux ropes in both cases are found to settle into a quasi-static rise. The evolution of the coronal magnetic field in the two cases remains nearly identical for most of this quasi-static rise (from $t = 90$ to about $t = 197$). Then the flux rope in case e1 reaches a critical height, after which it accelerates and results in a dynamic ejection of the flux rope. In contrast, the quasi-static rise of the flux rope in case s1 does not reach this critical height before it begins to fall back down again quasi-statically. The side-by-side evolution of the 3D coronal magnetic field of the two cases is also available as an animation in the online version of the journal. It clearly shows the nearly identical evolution for the two cases during the emergence and the earlier quasi-static rise after the emergence is stopped, and the later divergent behavior of the two coronal flux ropes after the flux rope in case e1 has crossed the critical height.

Figure 3 shows the evolution of the rise velocity of the coronal flux rope as a function of the height of the axial field line of the flux rope for all of the simulations with varying $t_{\rm stp}$ and H_m (see Table 1). The axial field line we track to represent the center

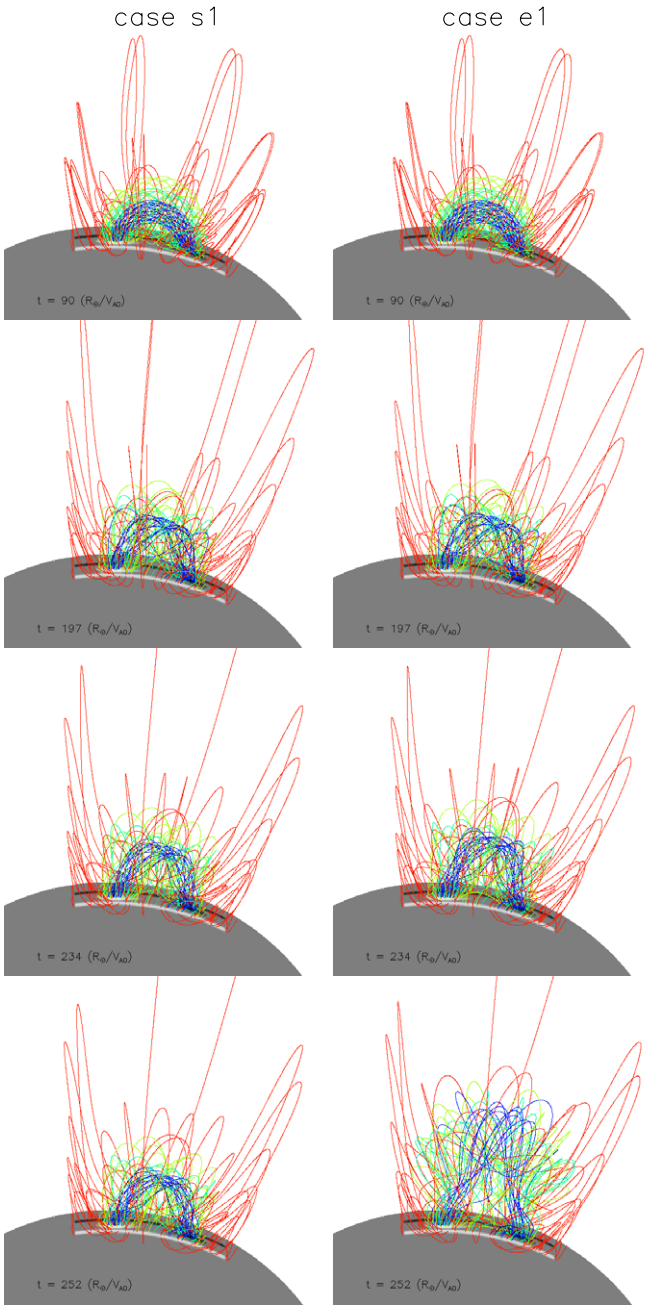

Figure 2. Side-by-side snapshots of the 3D coronal magnetic field evolution from two simulations, case s1 (left column) and case e1 (right column).

(An animation of this figure is available in the online journal.)

Table 1
Summary of Simulations

Case Label	$t_{stp}/\tau_{A0}(t_{stp}$ in s)	H_m/Φ^2 [a]	Erupts?
e5	91.0 (32469 s)	−0.20660	Yes
e4	90.0 (32112 s)	−0.20442	Yes
e3	89.5 (31934 s)	−0.20312	Yes
e2	89.25 (31844 s)	−0.20246	Yes
e1	89.125 (31800 s)	−0.20215	Yes
s1	89.0 (31755 s)	−0.20206	No
s2	88.0 (31398 s)	−0.19975	No

Note. [a] Total relative magnetic helicity normalized by the square of the total flux of one polarity threading through the surface.

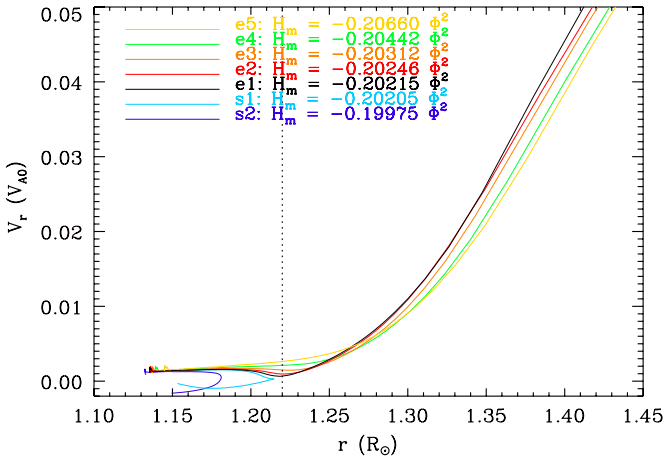

Figure 3. Evolution of the rise velocity of the flux rope as a function of the height of the axial field line of the flux rope, for all of the simulations (cases e5, e4, e3, e2, e1, s1, s2 in Table 1), each of which is represented by a different colored curve. The relative magnetic helicity reached by the coronal magnetic field at the time the emergence is stopped (normalized by the square of the total signed flux through the lower boundary) is also listed for each case, the same as that shown in the third column of Table 1.

of the flux rope does not remain the same field line (carrying the same plasma as would be the case under ideal frozen-in conditions) due to the small but finite numerical diffusion and the long quasi-static evolution. The way we track the axial field line is as follows. At t_{stp}, we determine the footpoints of the axis of the coronal flux rope as the intersections of the axis of the (prescribed) subsurface rising torus with the lower boundary. Then, (1) using one of the footpoints as the starting point, we trace out a field line in the coronal domain. In ideal conditions, this field line should go through the central vertical line of the domain and land on the other footpoint. But due to finite numerical diffusion, there is a slight deviation. (2) We then find the maximum height of the traced field line and use the point with that height on the central vertical line as the apex point to trace out a new field line, which we consider as the "axial field line" at the current time. This axial field line has two new footpoints which differ slightly from the original footpoints. These new footpoints of the current axial field line will then be used for the next output time step as the starting points to repeat the above procedure (steps (1) and (2)) again to determine the axial field line for the next time step, and so on. In ideal conditions, the footpoints for the axial field lines should remain fixed after t_{stp}. Due to the finite numerical diffusion in the simulation, the footpoints of the axial field line determined through the above procedure drift slightly on the lower boundary (by a few grid points) during the course of the quasi-static rise of the flux rope. On the other hand, the rise velocity of the flux rope in Figure 3 is determined by tracking (approximately) a Lagrangian element within the flux rope, and along the central vertical line of the domain, using only the velocity fields at the output times (the output interval is $\Delta t = 1\,R_\odot/v_{A0}$). The basic conclusion we draw from the results of Figure 3 is that there is a critical height (at $r \sim 1.22\,R_\odot$), if exceeded, the coronal flux rope becomes eruptive. If the coronal flux rope is unable to reach this height, it remains in a quasi-static state and eventually falls back down quasi-statically. The two cases shown in Figure 2 correspond to the light blue and black curves (cases s1 and e1). In Figure 4, we further show the acceleration of the flux rope as a function of the height of the axial field line of the flux rope for all the simulation cases (with the color of the points indicating the cases in the same way as that labeled for the curves in Figure 3). It shows

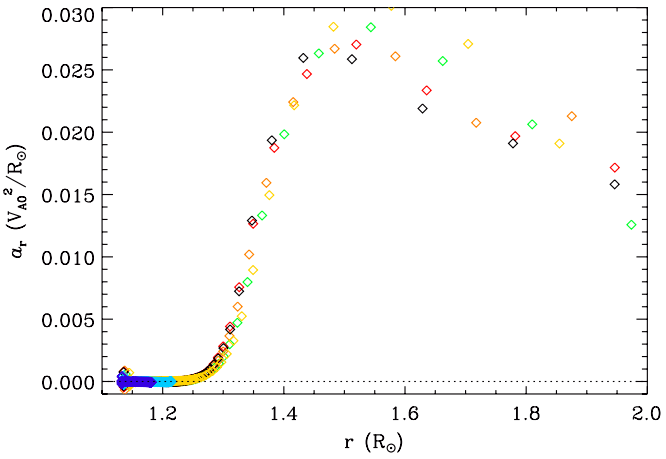

Figure 4. Acceleration of the flux rope as a function of the height of the axial field line of the flux rope, for all of the simulations, with the colors of the points indicating the cases e5, e4, e3, e2, e1, s1, s2 in the same way as that labeled for the curves in Figure 3.

that the transition from quasi-static evolution (with nearly zero a_r) to significant acceleration and dynamic eruption follows approximately the same height dependence for all the cases, even though their times for the onset of acceleration and eruption are very different (see Figure 5(a)). For those cases where the flux rope does not reach the critical height and eventually falls back down (light and dark blue points in Figure 4), the flux rope remains in a quasi-static state with nearly zero a_r.

At the critical height for the onset of eruption, the corresponding potential field B_p (with the same normal flux distribution on the lower boundary) declines with height h above the surface at a rate $-d\ln B_p/d\ln h \sim 1.74$. The above behavior of the eruption of the coronal flux ropes is consistent with the onset of the torus instability. The torus instability is fundamentally the expansion instability associated with a toroidal current ring confined by an external poloidal magnetic field (e.g., Bateman 1978; Kliem & Török 2006). The ring or torus experiences an outward "hoop force" due to the self-repulsion of the toroidal current, which is effectively an outward magnetic pressure gradient. This outward force is counteracted by an inward force due to the external poloidal field acting on the toroidal current. The expansion instability occurs if for a small increment $\delta\mathcal{R}$ of the major radius of the torus, the decline of the hoop force is slower than the decline of the confining force due to the external field and thus $\delta\mathcal{R}$ is amplified. This happens if the strapping, external field $B_{\rm ext}$ declines with the major radius $\mathcal{R}$ sufficiently rapidly, i.e., $n \equiv -d\ln B_{\rm ext}/d\ln\mathcal{R} > n_{\rm cr}$, where $n_{\rm cr}$ is a critical value. Different values of $n_{\rm cr}$ are obtained depending on how the toroidal current I varies with $\mathcal{R}$ during the expansion. If one assumes that the total number of field line turns in the torus remains constant during the outward expansion, then $n_{\rm cr} \approx 2$ is obtained (Titov & Demoulin 1999; Fan & Gibson 2007). If, on the other hand, magnetic reconnection sets in at the rear side of the expanding ring and lets the ring effectively "slide" through the external poloidal field, such that the sum of the flux induced by the toroidal current I and the flux of the fixed external poloidal field enclosed in the (expanding) toroidal current ring remains constant, then $n_{\rm cr} \approx 3/2$ is obtained (Bateman 1978; Kliem & Török 2006). However, the above derivations of $n_{\rm cr}$ for the torus instability is based on a freely expanding, two-dimensional axisymmetric toroidal current. The torus instability associated with a 3D line-tied, arched coronal flux rope is far more complicated. Isenberg & Forbes (2007) carried out a 3D

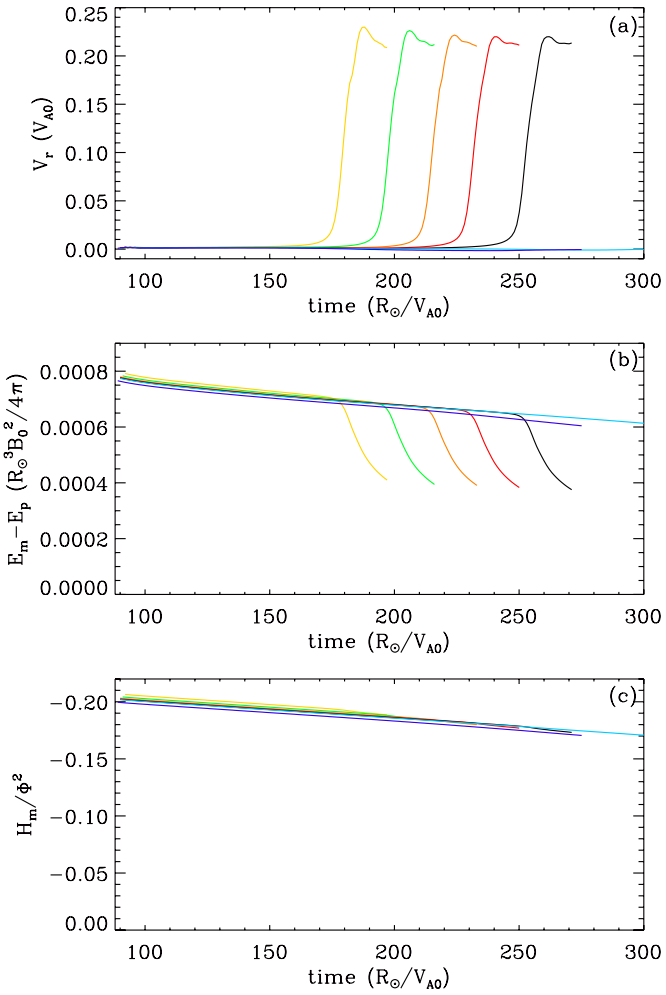

Figure 5. Temporal evolutions of (a) the rise velocity of the flux rope, (b) the free magnetic energy, i.e., the difference between the magnetic energy E_m and the corresponding potential magnetic field energy E_p, and (c) the relative magnetic helicity for all the cases (e5, e4, e3, e2, e1, s1, s2) with the different colored curves corresponding to the different cases as indicated in Figure 3.

analytical calculation of the stability of a line-tied coronal flux rope based on the equilibrium configuration described in Titov & Demoulin (1999). In this case, the coronal magnetic field is decomposed into a corresponding potential magnetic field B_p with the same normal flux distribution on the lower boundary, which remains fixed during eruption as a result of the line-tying lower boundary condition, and a completely detached coronal field generated by the flux rope's current in the corona and its image. Thus, here the hoop force that drives the flux rope outward is the self-force due to the current circuit formed by the flux rope current in the corona and its image, and the hoop force is counteracted by the confining force due to the potential field B_p acting on the coronal current. Therefore, crudely speaking, the height h of the coronal flux rope is a measure of the size of the current circuit and is analogous to the major radius $\mathcal{R}$ of the toroidal current described above, and B_p is the strapping field analogous to $B_{\rm ext}$ described above. By considering specific perturbations, Isenberg & Forbes (2007) found that the force equilibrium at the apex of the coronal flux rope is subject to the torus instability when the flux rope becomes sufficiently long, i.e., when the height h of the flux rope apex exceeds a critical value. For our set of simulations of the evolution of a 3D line-tied coronal flux rope confined by an arcade field, we also find that the condition for the onset of eruption is for the height

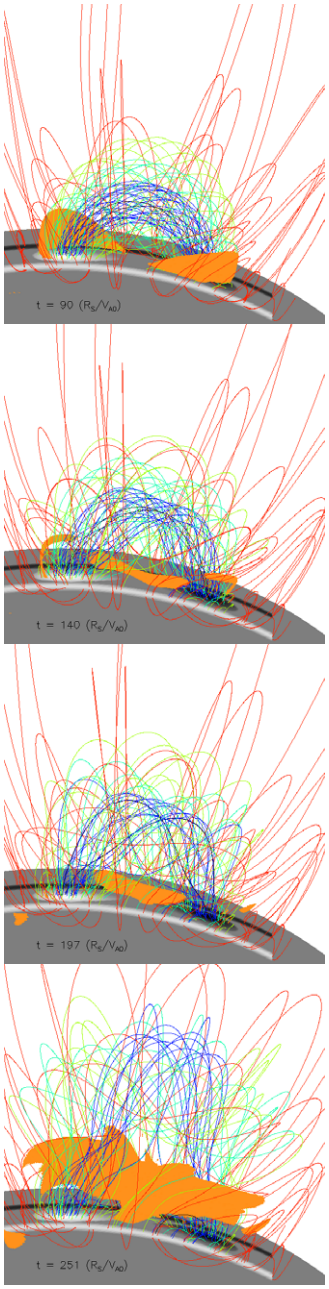

Figure 6. Iso-surfaces (orange surfaces) of $J/B = |\nabla \times \mathbf{B}|/B$, with the level set at $J/B = 1/l$ where $l = 10$ grid resolution elements, shown in relation to the 3D magnetic field lines at four time instances for case e1.

h of the flux rope to exceed a critical value. We find that $n_{\rm cr} \equiv -d \ln B_p / d \ln h$ at the critical height is about 1.74. In general, the critical height and the critical value $n_{\rm cr}$ should depend on the detailed normal flux distribution on the surface and the profile of the coronal flux rope.

Figure 5 shows the temporal evolution of (a) the rise velocity of the flux rope, (b) the free magnetic energy, and (c) the relative magnetic helicity of the coronal magnetic field, for all the cases (with the different colored curves corresponding to the different cases as indicated in Figure 3) after the emergence is stopped. We see that for the cases e5 through e1, the flux rope first settles into a quasi-static rise after the emergence is stopped, during which the magnetic energy decreases slowly (due to reconnections in the current layers forming under the flux ropes as is shown in the next section). Then the flux rope undergoes a sudden acceleration and erupts at different times for the different cases (see Figure 5(a)), which are determined by when the flux rope reaches the critical height (see Figure 4). For cases s1 and s2, the flux rope does not reach the critical height and remains in a quasi-static state. When the flux rope undergoes eruption, its free magnetic energy decreases significantly as shown in Figure 5(b). The decrease of the free magnetic energy during the eruption is much faster than the decrease of the magnetic helicity (see Figure 5(c)). The overall gradual decrease of the magnetic helicity after the emergence is stopped for all the cases seen in Figure 5(c) is due to the presence of the finite numerical diffusion of the magnetic field.

3.2. Current Sheets, Sigmoid Brightening, and Post-flare Loops

Figure 6 shows iso-surfaces (orange surfaces) of $J/B = |\nabla \times \mathbf{B}|/B$, outlining the region in the 3D magnetic field where J/B is above the level of $1/l$ with $l = 10$ grid resolution elements, at four time instances for the case e1. The iso-surfaces outline the formation of thin current layers which may, in realistic frozen-in evolution, correspond to sites of current sheet formation, where significant magnetic reconnections can take place. Figure 6 shows that current layers of sigmoid morphology, curving around and between the two legs of the flux rope, form in the quasi-static stage (see the first three panels which are during the quasi-static rise of the flux rope), and the current layer intensifies and extends upward during the onset of eruption (last panel). Magnetic reconnections take place in the current layers which cause the overall magnetic energy to decrease gradually during this quasi-static stage. Although the overall magnetic energy is declining, we find that the amount of the detached (twisted) magnetic flux associated with the flux rope is actually increasing during this quasi-static rise. We have computed this flux as

$$\Phi_{\rm detached} = \int (\mathbf{A} - \mathbf{A}_p) \cdot d\mathbf{l}, \tag{14}$$

where

$$\begin{aligned} \mathbf{A}_p(r,\theta,\phi) &= \nabla \times \left(\hat{\mathbf{r}} \int_r^\infty \psi(r',\theta,\phi) dr' \right) \\ &= -\frac{\hat{\theta}}{r} \int_r^\infty r' P_\phi(r',\theta,\phi) dr' \\ &\quad + \frac{\hat{\phi}}{r} \int_r^\infty r' P_\theta(r',\theta,\phi) dr' \end{aligned} \tag{15}$$

is the vector potential of the potential magnetic field $\mathbf{P} = -\nabla\psi$ having the same normal flux distribution on the lower boundary, and

$$\begin{aligned} \mathbf{A}(r,\theta,\phi) = &\frac{\hat{\theta}}{r} \left(-\int_{R_\odot}^\infty r' P_\phi(r',\theta,\phi) dr' + \int_{R_\odot}^r r' B_\phi(r',\theta,\phi) dr' \right) \\ &+ \frac{\hat{\phi}}{r} \left(\int_{R_\odot}^\infty r' P_\theta(r',\theta,\phi) dr' - \int_{R_\odot}^r r' B_\theta(r',\theta,\phi) dr' \right) \end{aligned} \tag{16}$$

is the vector potential of the coronal magnetic field $\mathbf{B}$. Thus $\mathbf{A} - \mathbf{A}_p$ is the vector potential of the completely detached magnetic field $\mathbf{B} - \mathbf{P}$ in the coronal domain, and the above integration in Equation (14) is carried out along the flux rope's axial field line, which is determined as described in Section 3.1 (see the discussion about Figure 3). Note also that in Equation (14) the integration only needs to be carried out along

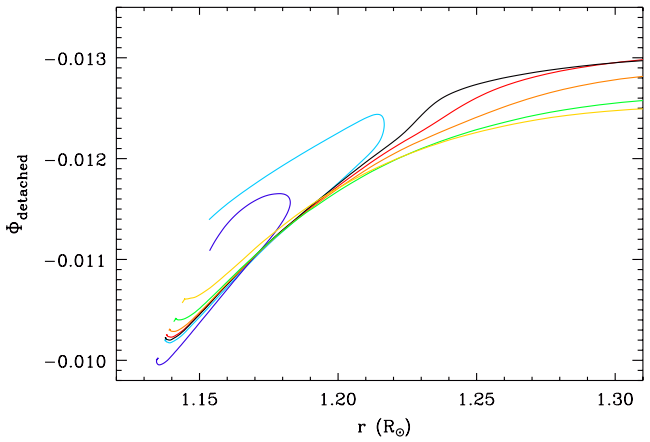

Figure 7. Detached flux $\Phi_{\rm detached}$ going under the axial field line of the flux rope (see the text for details), as a function of the apex height of the axial field line, for all the cases (e5, e4, e3, e2, e1, s1, s2) with the different colored curves corresponding to the different cases as indicated in Figure 3.

the axial field line in the domain, and does not need to be carried out along the line connecting the field line's footpoints on the lower boundary because $\mathbf{A} - \mathbf{A}_p = 0$ on the lower boundary. Thus, $\Phi_{\rm detached}$ computed from Equation (14) is the detached flux that threads through the area between the axial field line and the lower boundary. Since this flux is detached from the lower boundary (must close within the domain), it corresponds to the flux twisting about the axial field line in the domain. Figure 7 shows that in all the cases this detached flux twisting about the axial field line grows during the quasi-static rise (from $r \sim 1.15$ to the critical height of $r \sim 1.22$) of the flux rope after the emergence is stopped. In other words, reconnections during this stage add detached flux to the flux rope, allowing it to continue to rise because this detached flux enclosed under the *curved* axial field line and *pressed* against the lower boundary is the source of the outward magnetic pressure gradient (or the hoop force). For cases e1 through e5, the quasi-static rise of the flux rope exceeds the critical height of $r \sim 1.22$ and the flux rope then undergoes dynamic eruption, moving outward rapidly. On the other hand, for cases s1 and s2 (light blue and dark blue curves in Figure 7) the growth of $\Phi_{\rm detached}$ reaches a maximum before the flux rope gets to the critical height, and the flux rope eventually falls back down quasi-statically and $\Phi_{\rm detached}$ also decreases again.

Figure 8 traces out sampled field lines (pink field lines) that go through the current layers curving around and between the flux rope legs during the quasi-static rise. The current layers correspond to those outlined by the J/B iso-surfaces in the top three panels of Figure 6. Plasma along these field lines are expected to be preferentially heated due to magnetic energy dissipation in the current layers and may brighten up in X-ray, giving rise to the observed quiescent X-ray sigmoids before eruption (see the right column panels in Figure 8). This result has been found in many previous investigations (e.g., Titov & Demoulin 1999; Magara & Longcope 2001; Magara 2004; Gibson & Fan 2006; Archontis et al. 2009; Fan 2009).

At the onset of eruption, the central current layer between the two legs of the flux rope extends upward and the current density intensifies (see the bottom panel of Figure 6). Figure 9 (and the associated animation in the online version of the journal) shows sampled field lines (red field lines) whose tops are in the most intense part of the current layer (with $J/B = 1/l$ and $l < 4$ grid resolution elements) at a set of successive time instances during the eruption. These field lines correspond to the post-

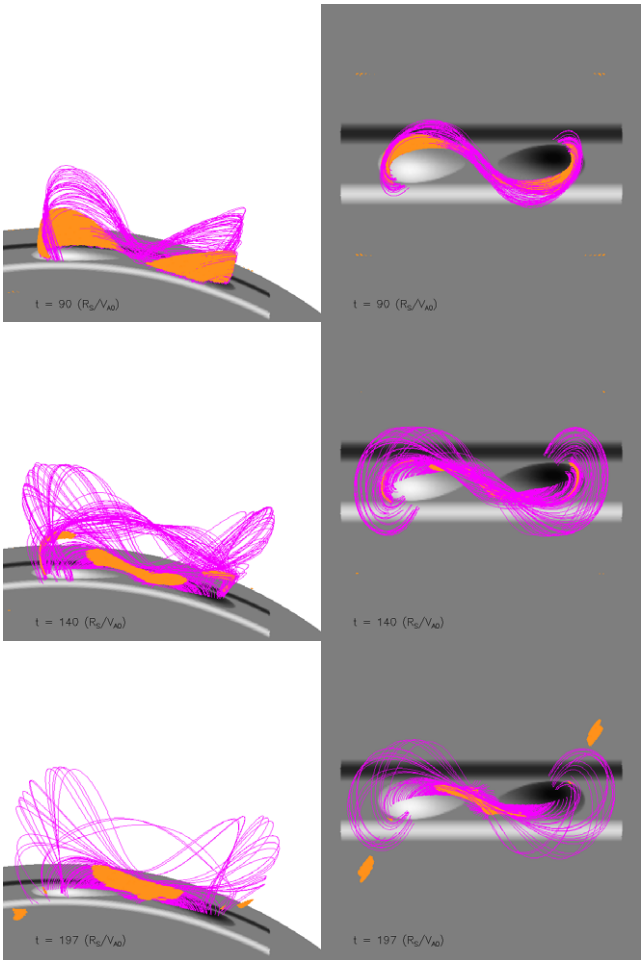

Figure 8. Two perspective views (left and right columns) of sampled field lines (pink field lines) going through the current layers outlined by the J/B iso-surfaces (orange surfaces, same as those shown in the top three panels of Figure 6), at three time instances during the quasi-static stage of case e1. The pink field lines collectively show a sigmoid morphology as can be seen from the top view in the right column.

flare loops which have just undergone reconnection in the most intensely driven part of the current layer. They are expected to be the most heated loops which indicate the morphology of the resulting X-ray brightening, and their footpoints would correspond to the locations of the chromospheric flare ribbons (red points in the right column panels). We can see (from the middle panels of Figure 9) that at the onset of eruption, the post-flare loops initially constitute a narrow, sigmoid-shaped bundle when viewed from the above, suggesting an initial narrow sigmoid (transient) brightening, which later broadens into a (curved) row of bright loops with increasing height. Such compact sigmoid-to-arcade transition of X-ray brightening is commonly observed during eruptive flares (e.g., Moore et al. 2001; Liu et al. 2007). When viewed from the side at certain angles, the post-flare loops display a cusp (see the left column panels in Figure 9). The evolution of the flare ribbons (see the right column of Figure 9) shows that they are initially compact sources on two sides of the polarity inversion line, and later they lengthen (in both directions) into two curved ribbons (showing sigmoid shape) and move apart from the polarity inversion line.

4. SUMMARY

We have carried out a sequence of MHD simulations of the evolution of the magnetic field in the corona where the

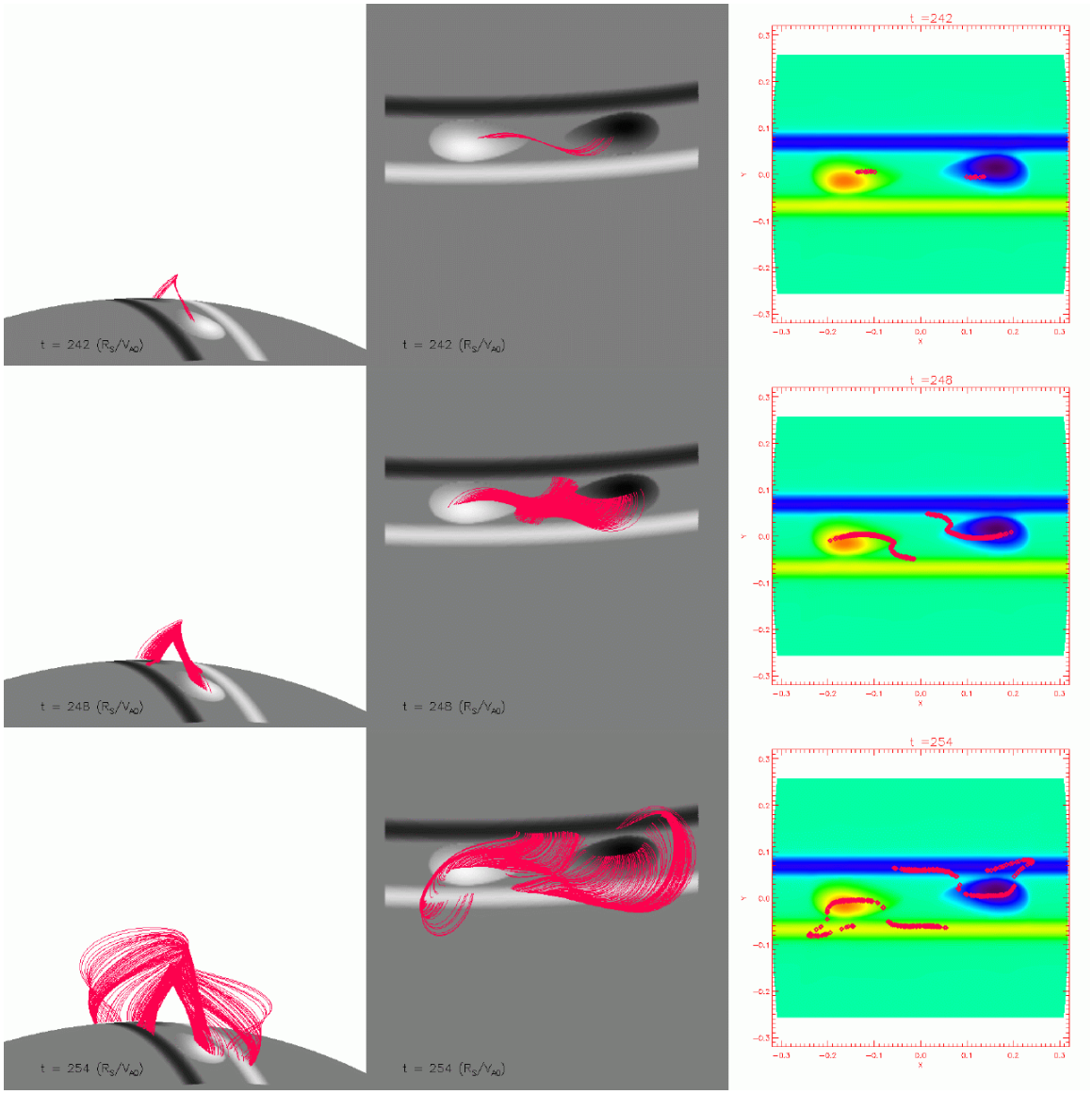

Figure 9. Two perspective views (left and middle columns) of sampled field lines (red field lines) whose tops are in the most intense part of the current layer (with $J/B = 1/l$ and $l < 4$ grid resolution elements), at three time instances during the eruption in case e1, indicating the morphology of the post-flare loops which have just undergone reconnection in the most intensely driven part of the current layer and whose footpoints correspond to the location of the chromospheric flare ribbons (red points in the right column panels). The gray-scale images in the left and middle column panels and the color images in the right column panels show the normal magnetic field distribution B_r on the lower boundary with white and yellow-red representing positive B_r, and black and blue-black indicating negative B_r.

(An animation of this figure is available in the online journal.)

emergence of a twisted magnetic flux tube is driven at the lower boundary into a pre-existing coronal arcade field, and the emergence is stopped at a variable time when a different amount of the twisted flux of the flux tube has been driven into the corona. The aim is to study the critical conditions for the onset of dynamic eruption of the coronal magnetic field. For all the simulation cases, a quasi-equilibrium line-tied coronal flux rope confined by the external arcade field is established after the emergence is stopped and the coronal flux rope is found to subsequently undergo a phase of quasi-static rise. In some of the cases (e1 through e5), the quasi-static rise is able to bring the flux rope to a critical height, at which the flux rope undergoes a sudden acceleration, and a dynamic eruption of the flux rope ensues. While in the other cases (s1 and s2), the flux rope does not reach the critical height, and it eventually falls back down again, quasi-statically. The onset of significant acceleration for the eruptive cases (e1 through e5) takes place at various different times (Figure 5), all depending on when the critical height is reached, i.e., it all follows approximately a single height dependence (see Figure 4). We find that the onset of eruption in these simulations is consistent with the onset of the torus instability of a coronal flux rope (e.g., Kliem & Török 2006; Titov & Demoulin 1999; Isenberg & Forbes 2007), which takes place when a critical height is reached where the outward hoop force of the flux rope can no longer be balanced by the confining force produced by the corresponding potential field due to the sufficiently steep rate of decline of the potential field. We find from these simulations that the decline rate of the corresponding potential field at the critical height is $n_{\rm cr} = -d \ln B_p / d \ln h \sim 1.74$, which is within the range of $n_{\rm cr}$ derived for the torus instability of an axisymmetric current ring (e.g., Bateman 1978; Kliem & Török 2006; Titov & Demoulin 1999; Fan & Gibson 2007). It is expected that the critical value $n_{\rm cr}$ for the onset of the torus instability for a 3D line-tied coronal

flux rope (such as that in our simulations) should vary with the detailed normal flux distribution on the line-tying lower boundary as well as the detailed profile of the coronal flux rope. Extensive 3D simulations for different field configurations are needed to investigate how the critical height and the value n_{cr} vary.

We find that during the quasi-static rise phase after the emergence is stopped, current layers of sigmoid morphology, curving around and between the two legs of the coronal flux rope, are formed. Reconnections in the current layers cause a gradual decrease of the total magnetic energy. (Note that after the emergence is stopped, there are no more Poynting flux and magnetic helicity flux driven through the lower boundary into the corona.) However, we also find that the reconnections during this initial quasi-static phase add detached (twisted) flux to the flux rope. This detached flux enclosed under the *curved* axial field line and *pressed* against the lower boundary is what gives rise to the outward magnetic pressure gradient (or the hoop force). Thus, the addition of the detached flux to the flux rope through reconnections contributes to its continued rise during this initial quasi-static phase, and if the quasi-static rise exceeds the critical height for the onset of the torus instability, then the flux rope erupts dynamically. This result is consistent with the conclusion drawn by a previous numerical study of a coronal flux rope driven by photospheric shear and flux cancellation by Aulanier et al. (2010), where they find that photospheric flux cancellation and tether-cutting coronal reconnection are not the cause of the eruption but are pre-eruption mechanisms for the flux rope to grow and rise to the critical height at which the torus instability causes the eruption. Here, our sequence of MHD simulations of coronal flux ropes formed by variable flux emergence clearly demonstrates that the critical condition for the onset of dynamic eruption of the coronal flux rope is to reach a critical height in the corona. We show that reconnections in the current layers underlying the coronal flux ropes during the initial quasi-static phases add detached flux to the coronal flux ropes, and thus are means to allow the flux ropes to rise to the critical height for the onset of the torus instability.

By tracing out sampled field lines that go through the sigmoid-shaped current layers underlying the flux rope during the pre-eruption quasi-static stage, we argue that these field lines, which all show a sigmoid morphology, may correspond to the observed quiescent X-ray sigmoid loops often seen in pre-eruption CME source regions (e.g., Rust & Kumar 1996; Canfield et al. 1999; Moore et al. 2001). Such an interpretation of the quiescent X-ray sigmoids has been given in many previous models of coronal flux ropes produced by flux emergence (e.g., Titov & Demoulin 1999; Magara & Longcope 2001; Magara 2004; Gibson et al. 2006; Archontis et al. 2009; Fan 2009). At the onset of eruption, we find that the central current layer between the two legs of the flux rope extends upward and the current density intensifies. By identifying field lines corresponding to the most heated post-flare loops which have just undergone reconnection in the most intensely driven part of the current layer, we deduce the morphology of the resulting X-ray brightening. We find that at the onset of eruption, the post-flare loops initially form a narrow sigmoid-shaped bundle when viewed from above, suggesting a narrow, transient sigmoid brightening, which then broadens into a (curved) row of loops, with increasing height. When viewed from the side at certain angles, the post-flare loops display a cusp. Based on the evolution of the footpoints of the post-flare loops, we deduce that the chromospheric flare ribbons evolve from initially a pair of compact sources into two curved ribbons (showing sigmoid shapes), which move apart on two sides of the polarity inversion line. The above qualitative features with regard to the evolution of the X-ray brightening and chromospheric flare ribbons deduced based on the evolution of the coronal magnetic field are consistent with some of the common features observed during eruptive flares taking place in regions with pre-existing X-ray sigmoids.

Y. Fan thanks M. Rempel and an anonymous referee for reviewing the manuscript and for helpful comments. The National Center for Atmospheric Research (NCAR) is sponsored by the National Science Foundation. This work is also supported in part by the NASA LWS TR&T grant NNX09AJ89G to NCAR. The numerical simulations were carried out on the Pleiades supercomputer at the NASA Advanced Supercomputing Division under award no. SMD-09-1282, project GID s0969.

REFERENCES

Amari, T., Luciani, J. F., Aly, J. J., Mikic, Z., & Linker, J. 2003, ApJ, 595, 1231
Amari, T., Luciani, J. F., Mikic, Z., & Linker, J. 2000, ApJ, 529, L49
Antiochos, S. K., DeVore, C. R., & Klimchuk, J. A. 1999, ApJ, 510, 485
Archontis, V., & Hood, A. W. 2010, A&A, 514, 56
Archontis, V., Hood, A. W., Savcheva, A., Golub, L., & Deluca, E. 2009, ApJ, 691, 1276
Archontis, V., Moreno-Insertis, F., Galsgaard, K., Hood, A., & O'Shea, E. 2004, A&A, 426, 1047
Aulanier, G., Török, T., Demoulin, P., & DeLuca, E. 2010, ApJ, 708, 314
Bateman, G. 1978, MHD Instabilities (Cambridge, MA: MIT Press), 84
Berger, M. A., & Field, G. B. 1984, J. Fluid Mech., 147, 133
Canfield, R. C., Hudson, H. S., & McKenzie, D. E. 1999, Geophys. Res. Lett., 26, 627
Fan, Y. 2001, ApJ, 554, L111
Fan, Y. 2005, ApJ, 630, 543
Fan, Y. 2009, ApJ, 697, 1529
Fan, Y., & Gibson, S. E. 2007, ApJ, 668, 1232
Forbes, T. G., & Priest, E. R. 1995, ApJ, 446, 377
Forbes, T. G., et al. 2006, Space Sci. Rev., 123, 251
Gibson, S. E., & Fan, Y. 2006, J. Geophys. Res., 111, A12103
Gibson, S. E., Fan, Y., Török, T., & Kliem, B. 2006, Space Sci. Rev., 124, 131
Isenberg, P. A., & Forbes, T. G. 2007, ApJ, 670, 1453
Kliem, B., & Török, T. 2006, Phys. Rev. Lett., 96, 255002
Lin, J, Forbes, T. G., Isenberg, P. A., & Demoulin, P. 1998, ApJ, 504, 1006
Lites, B. W., Low, B. C., Martinez Pillet, V., Seagraves, P., Skimanich, A., Frank, Z. A., Shine, R. A., & Tsuneta, S. 1995, ApJ, 446, 877
Liu, C., Lee, J., Yurchyshyn, V., Deng, N., Cho, K.-s., Karlicky, M., & Wang, H. 2007, ApJ, 669, 1372
Low, B. C. 2001, J. Geophys. Res., 106, 25141
Mackay, D. H., & van Ballegooijen, A. A. 2001, ApJ, 560, 445
Mackay, D. H., & van Ballegooijen, A. A. 2005, ApJ, 621, L77
Magara, T. 2004, ApJ, 605, 480
Magara, T. 2006, ApJ, 653, 1499
Magara, T., & Longcope, D. W. 2001, ApJ, 559, L55
Manchester, W., Gombosi, T., DeZeeuw, D., & Fan, Y. 2004, ApJ, 610, 588
Mikić, Z., & Linker, J. A. 1994, ApJ, 430, 898
Moore, R. L., Sterling, A. C., Hudson, H. S., & Lemen, J. R. 2001, ApJ, 552, 833
Okamoto, T. J., et al. 2008, ApJ, 673, L215
Rempel, M., Schüssler, M., & Knölker, M. 2009, ApJ, 691, 640
Roussev, I. I., Forbes, T. G., Gombosi, T. I., Sokolov, I. V., DeZeeuw, D. L., & Birn, J. 2003, ApJ, 588, L45
Rust, D. M., & Kumar, A. 1996, ApJ, 464, L199
Stone, J. M., & Norman, M. L. 1992a, ApJS, 80, 753
Stone, J. M., & Norman, M. L. 1992b, ApJS, 80, 791
Sturrock, P. A., Weber, M., Wheatland, M. S., & Wolfson, R. 2001, ApJ, 548, 492
Titov, V. S., & Demoulin, P. 1999, A&A, 351, 707
Török, T., & Kliem, B. 2005, ApJ, 630, L97
Török, T., & Kliem, B. 2007, Astron. Nachr., 328, 743
van Ballegooijen, A. A., Cartledge, N. P., & Priest, E. R. 1998, ApJ, 501, 866
van Ballegooijen, A. A., Priest, E. R., & Mackay, D. H. 2000, ApJ, 539, 983